Cobalt modulated local electronic environment of NiCoMnCuFe high-entropy alloys for stable overall water splitting

Xuepeng Ni,[a] Jingyu Guan,[b] Caixia Ren,[a] Liyin Hou,[a] Min Dong,*[a] Yaqin Tian,[a] Xiaojuan Wang,[a] Xueying Wen,[a] Lixia Qi,[a] Ruifeng Chen,[d] Yazhou Wang,*[a] and Yong Zheng*[c]

[a] *School of Energy and Constructional Engineering, Shandong Huayu University of Technology, Dezhou, Shandong, 253034, P.R. China*

[b] *Beijing Institute of Nuclear Engineering, China Nuclear Power Engineering Co., Ltd, Beijing 100840, P.R. China*

[c] *College of Materials and Chemical Engineering, Key Laboratory of Inorganic Nonmetallic Crystalline and Energy Conversion Materials, China Three Gorges University, Yichang, 443002, P.R. China*

[d] *School of Chemical Engineering and Technology, Tianjin University, Tianjin 300350, P.R. China*

Corresponding author: Yong Zheng, Yazhou Wang, Min Dong
E-mail: zhengyong@ctgu.edu.cn, wyz199021@163.com, dongmin8632@163.com

Experiment section

Materials

Sodium nitrate ($NaNO_3$, ≥98.5%) was supplied by Shanghai Macklin Biochemical Co., Ltd. Analytical-grade sulfuric acid (H_2SO_4, AR), hydrochloric acid (HCl, AR), hydrogen peroxide (H_2O_2, 30%), and potassium permanganate ($KMnO_4$, ≥99.5%) were sourced from Sinopharm Group Chemical Reagent Co., Ltd. Graphite powder, along with chloroplatinic acid hexahydrate ($H_2PtCl_6 \cdot 6H_2O$, AR), was procured from Aladdin Ltd. The $Ni(NO_3)_2 \cdot 6H_2O$, $Co(NO_3)_2 \cdot 6H_2O$, $Mn(NO_3)_2 \cdot 4H_2O$, $Cu(NO_3)_2 \cdot 3H_2O$, and $Fe(NO_3)_3 \cdot 9H_2O$ were obtained from Aladdin Reagent (Shanghai) Co., Ltd., China. All chemicals were directly used without any further purification.

Preparation of NiCoMnCuFe/RGO

Graphene Oxide (GO) was prepared from natural graphite by a modified Hummers' method. [1] Typically, 2 g of natural graphite and 1 g of $NaNO_3$ were dispersed in 46 mL of concentrated H_2SO_4 in a round-bottomed glass flask under gentle stirring. After stirring for 60 min, 6 g of $KMnO_4$ was gradually added to the mixture while maintaining continuous agitation. Subsequently, the resulting suspension was diluted by the addition of 100 mL of distilled water, followed by 350 mL of H_2O_2. The obtained precipitate was collected by centrifugation and repeatedly washed with distilled water and 10 wt% aqueous HCl solution until neutral pH was reached. Finally, the product was dried in a vacuum oven at 60 °C for 12 h to obtain GO. Stoichiometric amounts of metal nitrates-$Ni(NO_3)_2 \cdot 6H_2O$, $Co(NO_3)_2 \cdot 6H_2O$, $Mn(NO_3)_2 \cdot 4H_2O$, $Cu(NO_3)_2 \cdot 3H_2O$ and $Fe(NO_3)_3 \cdot 9H_2O$-corresponding to a nominal concentration of 0.4 M for each salt in solution, were individually weighed and dissolved in 20 mL of deionized (DI) water in a glass beaker under magnetic stirring for 10 min to form a homogeneous metal-ion solution. Subsequently, 300 mg of pre-synthesized graphene oxide (GO) was gradually introduced into the above solution, followed by further stirring for 20 min to ensure uniform dispersion and intimate mixing. The resulting suspension was then subjected to freeze-drying to obtain the NiCoMnCuFe/GO precursor. The dried precursor was transferred into a quartz boat and placed in a tubular furnace for subsequent thermal

treatment. The pyrolysis/alloying process was conducted at 900 °C for 2 h under a flowing 5% H_2/ 95% Ar atmosphere with a heating ramp of 5 °C min^{-1} to induce *in-situ* reduction and alloy formation. After natural cooling to room temperature, a cobalt-modulated NiCoMnCuFe high-entropy alloy anchored on reduced graphene oxide (denoted as NiCoMnCuFe/RGO)

For comparison, using the same experimental strategy, a series of cobalt-modulated NiCoMnCuFe high-entropy alloys with systematically varied Co contents were synthesized by tuning the concentration of $Co(NO_3)_2 \cdot 6H_2O$ (0, 0.2, and 0.6 M) in the metal-ion precursor anchored on reduced graphene oxide. The resulting samples are denoted as NiMnCuFe/RGO, $NiCo_{0.2}$MnCuFe/RGO and $NiCo_{0.6}$MnCuFe/RGO, respectively. Additionally, the RGO was also synthesized *via* the same experimental strategy without any metal nitrates.

Structural and Morphological Characterization

The morphology and microstructural features of the three synthesized samples were characterized using field-emission scanning electron microscopy (FESEM, SU-8010) and high-resolution transmission electron microscopy (HRTEM, JEM-2100F). The crystal structure was examined by X-ray diffraction (XRD, Rigaku D/max 2550 V), while the surface chemical states and elemental compositions were analyzed via X-ray photoelectron spectroscopy (XPS, Escalab 250Xi).

Electrochemical Measurements

Electrochemical tests were performed on an Ivium electrochemical workstation using a conventional three-electrode configuration, consisting of A glassy carbon electrode (GCE) with a diameter of 5 mm, a graphite rod counter electrode and an Hg/HgO reference electrode (1.0 M KOH). For the preparation of catalyst ink, 2 mg catalysts powder and 10 μL of 5 % Nafion solution were dispersed in 490 μL of ethanol solution by sonication for 1 h to obtain a homogeneous ink. Then, 10 μL of the electrocatalyst ink was dropped onto the surface of GCE with a loading of 2 $mg_{metal} \cdot cm^{-2}$ and dried naturally at room temperature. All recorded potentials were converted to the reversible hydrogen electrode (RHE) scale, with calibration applied according to the relation E (*vs.* RHE) $=E_{Hg/HgO}+0.098+0.0591\times pH$ for measurements in

1.0 M KOH. The oxygen evolution reaction (OER) catalytic performance was assessed by linear sweep voltammetry (LSV) at a sweep rate of 5 $mV \cdot s^{-1}$. 95% i_R-compensation was applied to correct the ohmic potential drop. Interfacial charge-transfer characteristics were interrogated through electrochemical impedance spectroscopy (EIS) over a frequency window from 10^5 to 0.01 Hz.

To further quantify the electrochemically accessible active surface, cyclic voltammetry (CV) was conducted in 1.0 M KOH at sweep rates of 10-50 $mV \cdot s^{-1}$ within the non-faradaic potential region. The resulting capacitive current response was used to extract the double-layer capacitance (C_{dl}), which served as a descriptor for estimating the electrochemical surface area (ECSA), owing to the proportionality between C_{dl} and the density of exposed interfacial sites. The ECSA values were subsequently determined using the equation below:

$$ECSA = \frac{C_{dl}}{40\ \mu F\ cm^{-2}\ per\ cm^{2}_{ECSA}}$$

The TOF (turnover frequency) value was calculated from the number of active sites for each catalyst using the following formula:

$$\text{HER: TOF } (s^{-1}) = (j \times A)/(2 \times F \times n)$$

where j (A cm^{-2}) is the measured current density at different overpotentials, A is the electrode geometric surface area, F (96500 C mol^{-1}) is the Faraday constant, and n (mol) is the number of active sites obtained by CV method ($n = Q_s/F$). All CV tests were analyzed in PBS solution (pH = 7.4) at a scan rate of 50 $mV \cdot s^{-1}$. The surface charge (Q_s) was then calculated to be half of the integrated charge over the whole potential range.

Anion Exchange Membrane Water Electrolysis Test

Anion exchange membrane water electrolysis (AEMWE) measurement: The anode was NiCoMnCuFe/RGO, and the cathode was commercial Pt/C and IrO_2 with the accurate test area was 1 × 1cm. Both the cathode and anode were separated by a Fumasep FAA-3-PK-130 anion exchange membrane with a thickness of 130 μm. Further, NiCoMnCuFe/RGO was coated on 1 × 1 cm^2 carbon paper by ultrasonic

spraying, which work as the cathodes of the electrolyser (loading: 1mg cm^{-2}). The measurements were conducted at 25 °C, 50 °C and 80 °C in 1 M KOH electrolyte. The LSV curve was not corrected for the ohmic potential loss. AEMWE was tested by a constant current regulated power supply.

Theoretical calculation

The calculations were performed within the framework of density functional theory (DFT) using a plane-wave pseudopotential approach, as implemented in the Vienna Ab initio Simulation Package (VASP). The electron–ion interactions were described by projector-augmented wave (PAW) potentials. For the exchange–correlation functional, the Perdew–Burke–Ernzerhof generalized gradient approximation (PBE-GGA) was employed. Prior to the main simulations, convergence tests were conducted for the plane-wave cutoff energy and the k-point sampling. The cutoff energy of 450 eV was adopted. The Monkhorst-Pack method was applied to perform the Brillouin zone integrations, in which the k-point values of 3 × 3 × 1 was used for structural optimization. An additional ~15 Å thick vacuum regime and a dipole correction scheme were introduced to the slab models to electrostatically isolate the surface model from periodic images.

The change in Gibbs free energy (ΔG) for each possible steps was obtained from the following equation:

$$\Delta G = \Delta E + \Delta E_{ZPE} - T\Delta S$$

Where ΔE is the reaction energy obtained by analyzing the DFT total energies. ΔE_{ZPE} is the zero-point energy change, which is obtained from vibrational frequencies. ΔS is the change in entropy between the products and the reactants at room temperature (T = 298.15 K)

The HER performance is quantified by the reaction Gibbs free energy of hydrogen adsorption. The closer $|\Delta G_H|$ is zero, the better the HER performance in principle.

The OER mechanism can be described by 4 steps using the equations below:

$$OH^- + * \rightarrow OH* + e^- \quad (1)$$

$$OH* + OH^- \rightarrow O* + H_2O + e^- \quad (2)$$

$$O* + OH^- \rightarrow OOH* + e^- \quad (3)$$

$$OOH* + OH^- \rightarrow * + O_2 + H_2O + e^- \quad (4)$$

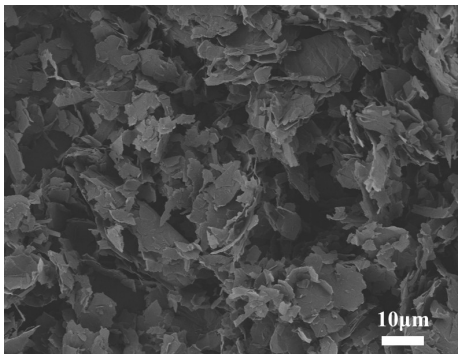

Fig. S1. SEM image of bare RGO.

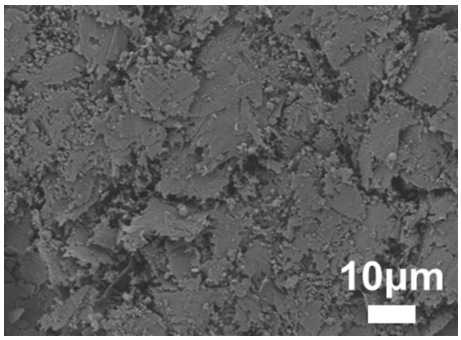

Fig. S2. SEM image of NiCoMnCuFe/RGO.

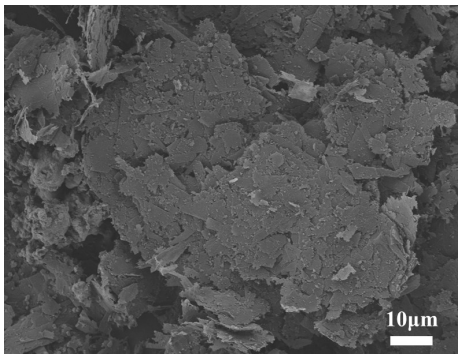

Fig. S3. SEM image of NiMnCuFe/RGO.

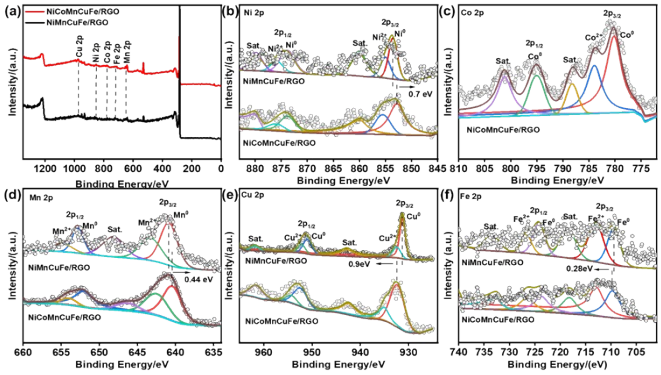

Fig. S4. XPS spectra comparison of NiCoMnCuFe/RGO and NiMnCuFe/RGO: (a) survey, (b) core-spectra Ni 2p, (c) Co 2p, (d) Mn 2p, (e) Cu 2p, and Fe 2p.

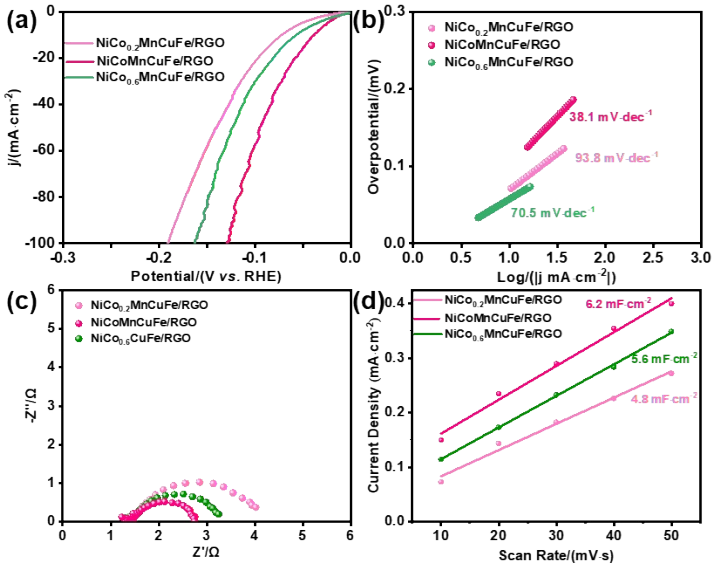

Fig. S5. The HER performance with different Co-doping amounts.

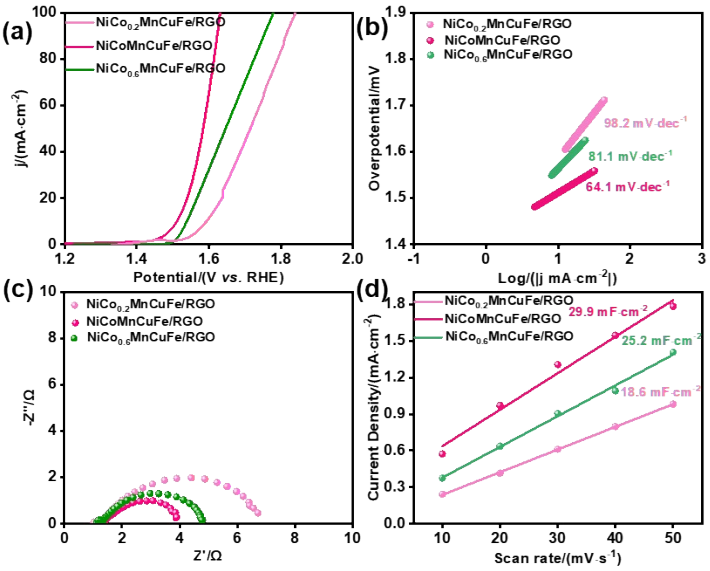

Fig. S6. The OER performance with different Co-doping amounts.

We first examined the effect of Co content on the HER and OER performances (Fig. S5-6). The catalytic activity of NiCoMnCuFe/RGO exhibits a clear dependence on the Co concentration, with both insufficient and excessive Co incorporation leading to inferior activity. This trend indicates that an appropriate level of Co incorporation is essential for effectively modulating the local electronic environment and maximizing the synergistic effect for high entropy alloys.

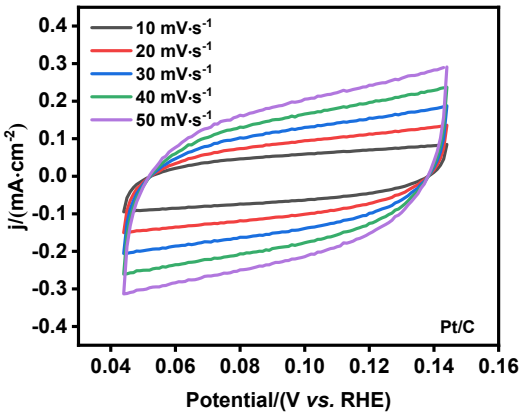

Fig. S7. The CV curve of Pt/C at different scan rates.

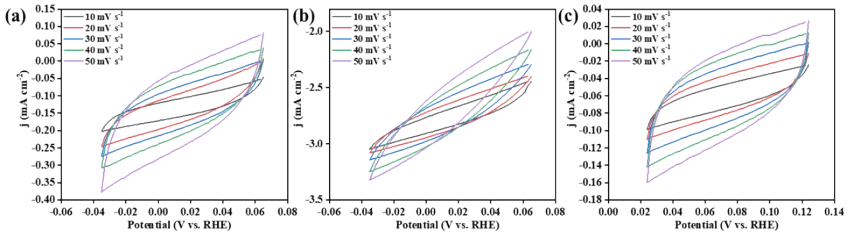

Fig. S8. The HER performance: The CV curve of (a) NiMnCuFe/RGO, (b) NiCoMnCuFe/RGO and (c) RGO.

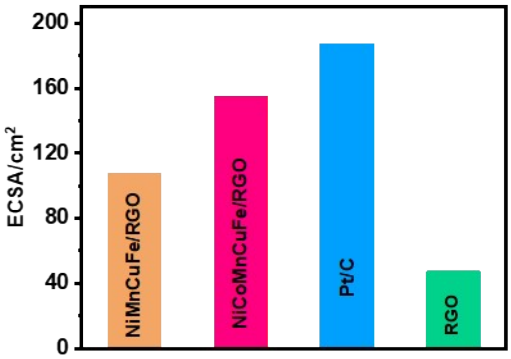

Fig. S9. The ECSA of NiMnCuFe/RGO, NiCoMnCuFe/RGO, RGO and Pt/C.

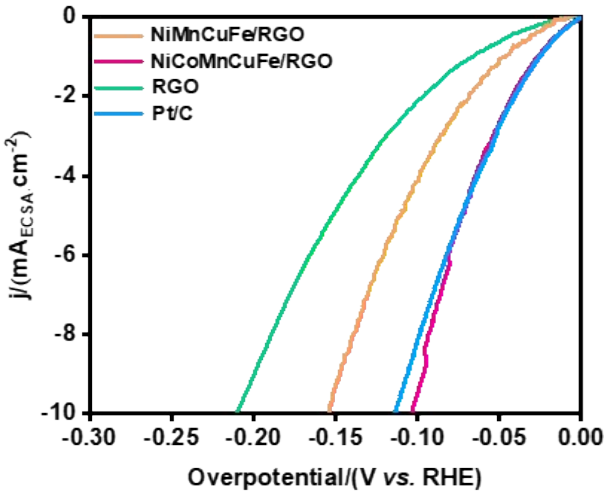

Fig. S10. The ECSA-normalized HER polarization curves of different catalysts.

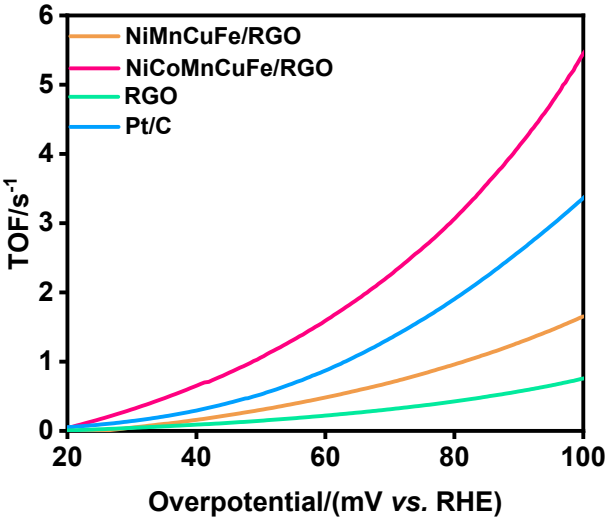

Fig. S11. The relationship between TOF and the overpotential of different catalysts.

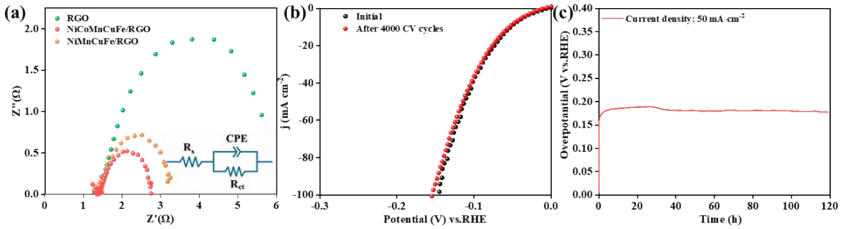

Fig. S12. The HER performance: (a) EIS plots of NiCoMnCuFe/RGO, NiMnCuFe/RGO, and RGO; (b) LSV curves before and after 4000 CV cycles, and (c) durability test at 50 $mA \cdot cm^{-2}$ of NiCoMnCuFe/RGO.

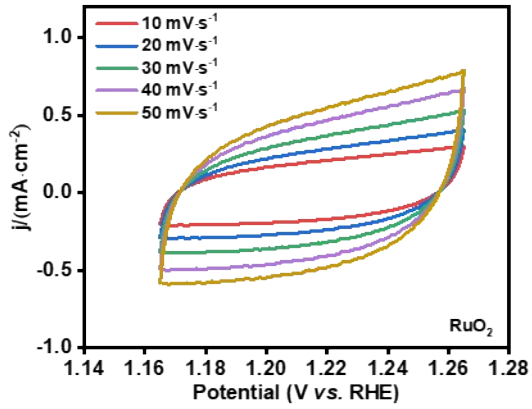

Fig. S13. The CV curve of RuO_2 at different scan rates.

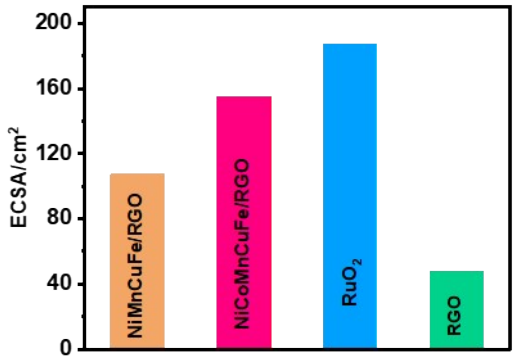

Fig. S14. The ECSA of NiMnCuFe/RGO, NiCoMnCuFe/RGO, RGO and RuO_2.

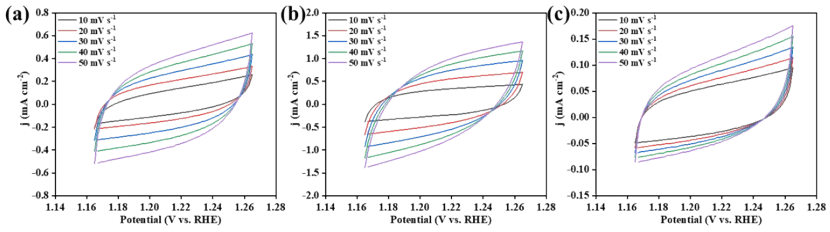

Fig. S15. The OER performance: The CV curve of (a) NiMnCuFe/RGO, (b) NiCoMnCuFe/RGO, and (c) RGO.

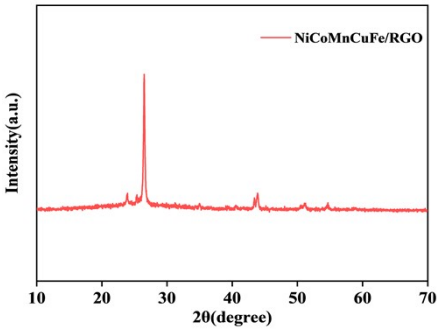

Fig. S16. XRD patterns of NiCoMnCuFe/RGO after after AEMWE durability test.

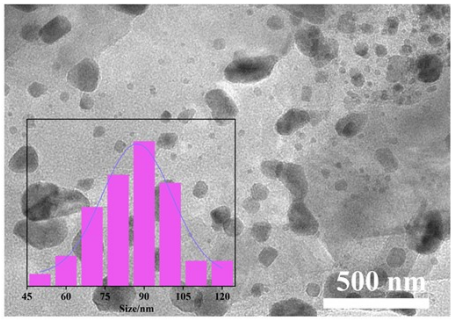

Fig. S17. TEM images of of NiCoMnCuFe/RGO after after AEMWE durability test. Illustration is Particle size distribution curve.

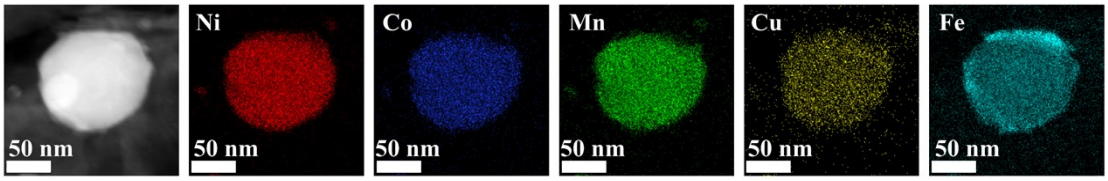

Fig. S18. HR-TEM image and EDS mappings of NiCoMnCuFe/RGO after AEMWE durability test.

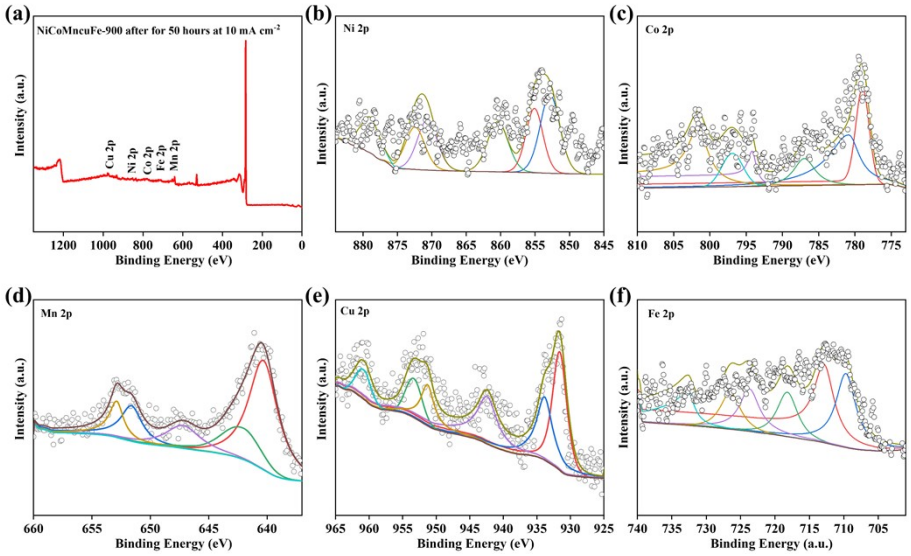

Fig. S19. XPS spectra of NiCoMnCuFe/RGO after AEMWE durability test: (a) survey, (b) core-spectra Ni 2p, (c) Co 2p, (d) Mn 2p, (e) Cu 2p, and Fe 2p.

As shown in Fig. S16, the phase composition of the NiCoMnCuFe/RGO electrode remains essentially unchanged after long-term electrolysis, with the face-centered cubic phase still being dominant, indicating good phase stability. The TEM image in Fig. S17 shows that the overall nanostructure remains uniformly distributed throughout the sample, with an average particle size of approximately 90 nm, which is only about 10 nm larger than that of the pristine catalyst. The corresponding elemental mapping results (Fig. S18) further confirm that the catalyst retains a homogeneous solid-solution structure after the stability test. Moreover, the post-stability XPS spectra (Fig. S19) exhibit negligible changes in both elemental composition and oxidation states compared to the pristine catalyst, suggesting excellent chemical stability under prolonged electrolysis conditions.

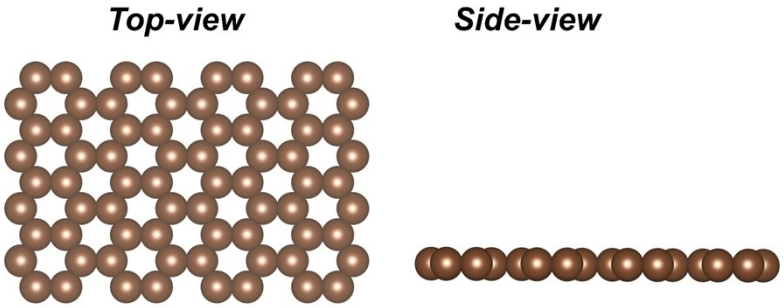

Fig. S20. Optimized bare RGO structural model presented in top and side-view configurations.

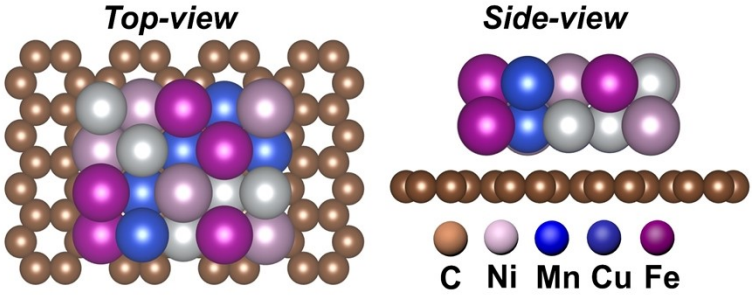

Fig. S21. Optimized NiMnCuFe/RGO structural model presented in top- and side-view configurations.

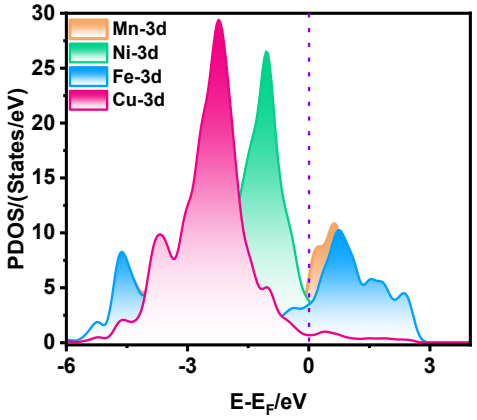

Fig. S22. PDOS analysis of the NiMnCuFe/RGO catalyst.

1. F. Ghasemi and M. H. Amiri, *Appl. Surf. Sci.*, 2021, **570**, 151228.